Accurate Modeling of Body Area Network Channels Using Surface-Based Method of Moments

Ahmed M. Eid and Jon W. Wallace, *Member, IEEE*

***Abstract*—An accurate method for modeling body shadowing in body area networks (BANs) is presented, based on an efficient surface-based method-of-moments (MOM) solution. The method allows the fields radiated by a transmit line current with arbitrary orientation (polarization) in the presence of a lossy dielectric cylinder of arbitrary cross section to be computed with high accuracy. The fields due to a point source are then found using Fourier transform techniques. The utility of the method for BAN modeling is demonstrated by comparing with BAN measurements on a human subject performed in a compact chamber and in an open field.**

***Index Terms*—Biological systems, method of moments, modeling, propagation.**

I. Introduction

BODY AREA networks (BANs) are an emerging paradigm for wireless communications where communicating nodes are placed near or inside the body, with applications in biomedicine, sports, emergency response, and consumer electronics. Although such sensors can be connected by wired links, wireless BANs provide more freedom of movement for the user or patient. However, designing wireless BAN systems that are robust, efficient, and high performance is challenging since the body forms an integral part of the antennas and propagation channel. The purpose of this paper is to develop a model for on-body communications that is not only simple and accurate, but also as general as possible in accommodating different antenna types and environments.

In [1] it was identified that propagation between two shadowed BAN nodes can occur due to waves penetrating through the body or creeping around the body, but that the creeping waves dominate in most cases. BAN characterization has been achieved by measurements [2]–[4], as well as detailed simulations [1]. Although these studies successfully assess BAN communications for a specific type of antenna and environment, one drawback of these approaches is that the observations are antenna and environment specific, possibly limiting the generality of the results.

An important recent step toward antenna- and environment-independent characterization is provided by [5], which models the body as an infinite lossy dielectric cylinder with circular cross section, derives the scattered fields due to a $\hat{z}$-directed (along axis) current source using conventional modal analysis, and derives the response to a point source using a Fourier transform. The model was extended in [6] for arbitrary polarization and compared with measurements in a compact anechoic chamber, revealing good agreement for some polarizations, but poor agreement for others.

The purpose of this paper is to take the approach in [5] one step further by modeling the body as an infinite cylinder with *arbitrary* cross section, since the body shape and curvature can play a vital role for certain antennas and polarizations. The natural choice taken herein is to consider surface-based method-of-moments (MOM) [7]–[9], where the only unique unknowns are tangential fields at the air-body interface. Although such developments are slightly more complicated than simple traditional volume-based approaches that segment the interior of the scatterer [10], [11], the surface-based approach only requires segmentation of the air-body surface, leading to significant improvement in efficiency. In the paper, a compact and self-contained derivation of the surface-based MOM approach for BAN is provided, not only to make the method as accessible and complete as possible for the BAN research community, but also to help generalize and simplify existing treatments. Additionally, measurements are performed both in a compact anechoic chamber and in an open outdoor range to check the accuracy of the proposed model.

The organization of the paper is as follows: Section II develops the surface-based method-of-moments solution for BAN modeling, and in Section III it is validated and different torso models are presented. Section IV then compares the model with on-body measurements taken in an anechoic chamber and outdoors. Finally, Section V concludes the paper.

II. Surface-Based Numerical Solution for BAN Propagation

Fig. 1 depicts a lossy dielectric cylinder model of the body, whose shape varies only in the xy plane and is infinite and homogeneous in the z-direction. The perimeter of the object is defined by the contour C. It is required to calculate the field at observation point (x, y) in response to a point current source of arbitrary orientation with density

$$\overline{J} = \delta(x - x_0)\delta(y - y_0)\delta(z - z_0)(a_x\hat{x} + a_y\hat{y} + a_z\hat{z}). \quad (1)$$

The problem is solved using the approach in [5], where first the fields due to a line source with current density

$$\overline{J} = \delta(x - x_0)\delta(y - y_0)(a_x\hat{x} + a_y\hat{y} + a_z\hat{z})\exp(-jk_z z) \quad (2)$$

Manuscript received September 30, 2010; revised December 17, 2010; accepted December 28, 2010. Date of publication June 09, 2011; date of current version August 03, 2011.

The authors are with the School of Engineering and Science, Jacobs University, 28759 Bremen, Germany (e-mail: ahmedmossa@hotmail.com; wall@ieee.org).

Color versions of one or more of the figures in this paper are available online at http://ieeexplore.ieee.org.

Digital Object Identifier 10.1109/TAP.2011.2158971

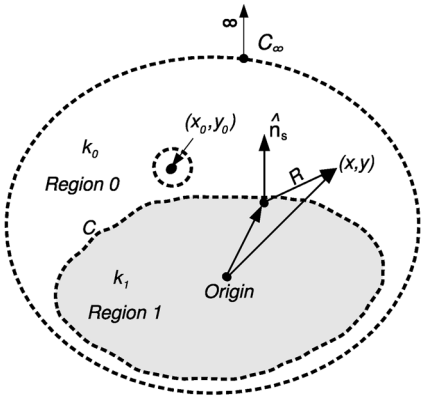

Fig. 1. Arbitrarily shaped biological body illuminated by an external source.

are obtained, which can then be transformed via Fourier techniques to find the point source solution.

We note that surface-based MOM solutions for an infinite dielectric cylinder with arbitrary cross-section are well known [7]–[9], and are closely related to the problem here of solving for fields radiated by the line current (2) in the presence of the lossy cylinder. However, directly applying these previous treatments is difficult due to existing limitations that are not trivial: lack of generality (i.e. single polarization), restriction to plane-wave excitation (usually normal incidence), and the absence of the $\exp(-jk_z z)$ variation.

Instead of trying to remedy or extend existing treatments, the approach taken in this work is to develop a compact and unified approach that directly exploits the $\exp(-jk_z z)$ variation of fields as is done in waveguide analysis, and as is shown, this novel approach results in a very compact and elegant solution for BAN modeling.

A. Governing Equations

In a homogeneous region without sources, electric $(\overline{E})$ and magnetic $(\overline{H})$ field satisfy

$$[\nabla^2 + k^2]\{\overline{E}, \overline{H}\} = 0 \tag{3}$$

where k is the wavenumber of the medium.

Since the line source has $\exp(-jk_z z)$ variation and the geometry is homogeneous in z, the solutions for $\overline{E}$ and $\overline{H}$ must also have $\exp(-jk_z z)$ variation. As in waveguide analysis, this form allows fields transverse to the z direction to be written as

$$\overline{E}_T = \frac{-j}{k_\rho^2}(k\eta \nabla_T \times \hat{z} H_z + k_z \nabla_T E_z) \tag{4}$$

$$\overline{H}_T = \frac{j}{k_\rho^2}\left(\frac{k}{\eta}\nabla_T \times \hat{z} E_z - k_z \nabla_T H_z\right) \tag{5}$$

where $k_\rho^2 = k^2 - k_z^2$, which means that E_z and H_z are the only unique unknowns, and in the ith homogeneous region, the two-dimensional relationship

$$\left[\nabla_T^2 + k_{\rho i}^2\right]\{E_z, H_z\} = 0 \tag{6}$$

holds, where $\nabla_T = \hat{x}\partial/\partial x + \hat{y}\partial/\partial y$ is a two-dimensional transverse operator and $k_{\rho i}^2 = k_i^2 - k_z^2$. The solution to the problem

$$\left[\nabla_T^2 + k_{\rho i}^2\right] g_i(\overline{\rho}, \overline{\rho}') = \delta(x - x')\delta(y - y') \tag{7}$$

is given by the usual two-dimensional scalar Green's function

$$g_i(\overline{\rho}, \overline{\rho}') = \frac{j}{4} H_0^{(2)}\left(k_{\rho i}|\overline{\rho} - \overline{\rho}'|\right) \tag{8}$$

and combining (8) and (6) with Green's theorem, yields

$$E_{zi}(\overline{\rho}) = \int_{\partial S_i} \left[E_{zi}(\overline{\rho}')\frac{\partial g_i(\overline{\rho}, \overline{\rho}')}{\partial n'} - g_i(\overline{\rho}, \overline{\rho}')\frac{\partial E_{zi}(\overline{\rho}')}{\partial n'}\right] d\ell' \tag{9}$$

where E_{zi} is E_z in the ith region, ∂S_i is the contour formed by the boundary of the homogeneous region S_i, $\hat{n}'$ is the normal vector on the contour at point $\overline{\rho}'$ outward from S_i, and the same equation holds for H_z. For a region S_i defined to lie inside multiple unconnected boundaries, (9) still holds where ∂S_i includes all boundaries and $\hat{n}'$ is always away from the medium S_i. Note that the observation point in (9) must be strictly inside S_i.

Fields in Region 0 (outside the body) are found by writing (9) with closed contours around the line source, around the body, and at infinity (far-field), as depicted in Fig. 1. The contour around the line source just yields fields radiated by the line source in free space, and the contour integral at infinity vanishes, leaving

$$E_{z0}(\overline{\rho}) = E_{z0}^{\text{inc}}(\overline{\rho}) + E_{z0}^{\text{scat}}(\overline{\rho}) \tag{10}$$

$$E_{z0}^{\text{scat}}(\overline{\rho}) = -\oint_C \left[E_{z0}(\overline{\rho}')\frac{\partial g_0(\overline{\rho}, \overline{\rho}')}{\partial n_s'} - g_0(\overline{\rho}, \overline{\rho}')\frac{\partial E_{z0}(\overline{\rho}')}{\partial n_s'}\right] d\ell' \tag{11}$$

where $\hat{n}_s'$ is the outward normal direction from the scatterer (the body) and the sign change comes from $\hat{n}_s' = -\hat{n}'$ in Region 0. Fields in Region 1 (inside the body) are given by the single contour integral

$$E_{z1}(\overline{\rho}) = \oint_C \left[E_{z1}(\overline{\rho}')\frac{\partial g_1(\overline{\rho}, \overline{\rho}')}{\partial n_s'} - g_1(\overline{\rho}, \overline{\rho}')\frac{\partial E_{z1}(\overline{\rho}')}{\partial n_s'}\right] d\ell'. \tag{12}$$

B. Incident Fields

Incident electric $(\overline{E}^{\text{inc}})$ and magnetic $(\overline{H}^{\text{inc}})$ field due to a line source in free space is given in [6] and for brevity is not repeated here.

C. Boundary Conditions

Solving the governing equations requires enforcing the proper continuity conditions at the boundary. Although $H_{z0} = H_{z1}$ and $E_{z0} = E_{z1}$ on C, the normal derivatives $\partial H_z/\partial n_s$ and $\partial E_z/\partial n_s$ may be discontinuous on the boundary.

Let $\hat{n} = \hat{n}_s$ be the outward normal of the scatterer (orthogonal to $\hat{z}$) and $\hat{\ell} = \hat{z} \times \hat{n}$ be the vector tangential to the surface. The transverse field components satisfy the conditions

$$\begin{aligned} \hat{n} \times \overline{E}_{T0} &= \hat{n} \times \overline{E}_{T1} \qquad \hat{n} \cdot (\epsilon_0 \overline{E}_{T0}) = \hat{n} \cdot (\epsilon_1 \overline{E}_{T1}) \\ \hat{n} \times \overline{H}_{T0} &= \hat{n} \times \overline{H}_{T1} \qquad \hat{n} \cdot \overline{H}_{T0} = \hat{n} \cdot \overline{H}_{T1}. \end{aligned} \tag{13}$$

Considering (4), (5), the required operations

$$\begin{aligned} \hat{n} \times (\nabla_T \times \hat{z} f) &= -\hat{z} \frac{\partial f}{\partial n} \qquad \hat{n} \times (\nabla_T f) = \hat{z} \frac{\partial f}{\partial \ell} \\ \hat{n} \cdot (\nabla_T \times \hat{z} f) &= \frac{\partial f}{\partial \ell} \qquad \hat{n} \cdot (\nabla_T f) = \frac{\partial f}{\partial n} \end{aligned} \tag{14}$$

are easily derived, where f is an arbitrary function. Thus, substituting (4), (5) into (13) gives

$$\begin{aligned} &\frac{k_{\rho 1}^2}{k_{\rho 0}^2} \left(k_0 \eta_0 \frac{\partial H_{z0}}{\partial n} - k_z \frac{\partial E_{z0}}{\partial \ell} \right) \\ &\quad = k_1 \eta_1 \frac{\partial H_{z1}}{\partial n} - k_z \frac{\partial E_{z1}}{\partial \ell} \end{aligned} \tag{15}$$

$$\begin{aligned} &\frac{k_{\rho 1}^2 \eta_1^2}{k_{\rho 0}^2 \eta_0^2} \left(k_0 \eta_0 \frac{\partial H_{z0}}{\partial \ell} + k_z \frac{\partial E_{z0}}{\partial n} \right) \\ &\quad = k_1 \eta_1 \frac{\partial H_{z1}}{\partial \ell} + k_z \frac{\partial E_{z1}}{\partial n} \end{aligned} \tag{16}$$

$$\begin{aligned} &\frac{k_{\rho 1}^2}{k_{\rho 0}^2} \left(\frac{k_0}{\eta_0} \frac{\partial E_{z0}}{\partial n} + k_z \frac{\partial H_{z0}}{\partial \ell} \right) \\ &\quad = \frac{k_1}{\eta_1} \frac{\partial E_{z1}}{\partial n} + k_z \frac{\partial H_{z1}}{\partial \ell} \end{aligned} \tag{17}$$

$$\begin{aligned} &\frac{k_{\rho 1}^2}{k_{\rho 0}^2} \left(\frac{k_0}{\eta_0} \frac{\partial E_{z0}}{\partial \ell} - k_z \frac{\partial H_{z0}}{\partial n} \right) \\ &\quad = \frac{k_1}{\eta_1} \frac{\partial E_{z1}}{\partial \ell} - k_z \frac{\partial H_{z1}}{\partial n}. \end{aligned} \tag{18}$$

Note that the tangential derivatives $\partial H_z / \partial \ell$ and $\partial E_z / \partial \ell$ must be equal on the two sides of the interface, since everywhere on the contour $H_{z0} = H_{z1}$ and $E_{z0} = E_{z1}$. Using this fact the tangential derivatives can be eliminated from the equations, yielding

$$c_{h,0} \frac{\partial H_{z0}}{\partial n} = c_{h,1} \frac{\partial H_{z1}}{\partial n}, \quad c_{e,0} \frac{\partial E_{z0}}{\partial n} = c_{e,1} \frac{\partial E_{z1}}{\partial n} \tag{19}$$

where

$$c_{h,i} = \frac{1}{k_{\rho i}^2} \left(k_i \eta_i - k_z^2 \beta \right) \tag{20}$$

$$\beta = \left(\frac{k_0}{k_{\rho 0}^2 \eta_0} - \frac{k_1}{k_{\rho 1}^2 \eta_1} \right)^{-1} \left(\frac{1}{k_{\rho 0}^2} - \frac{1}{k_{\rho 1}^2} \right) \tag{21}$$

and $c_{e,i} = c_{h,i} / \eta_i^2$. Therefore, we only need to retain z-directed fields and normal derivatives on the outside surface as the unique unknowns, and substitute (19) for fields on the inside boundary. Also, note that since governing equations and boundary conditions for E_z and H_z are uncoupled, they can be solved for separately.

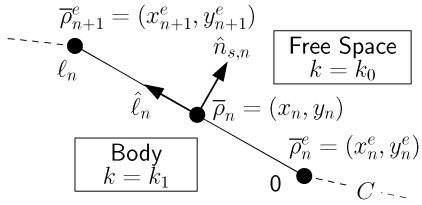

Fig. 2. The nth segment for the method-of-moments discretization procedure. Order of the endpoints is chosen so that when moving to the next endpoint, the outward normal of the scatterer $\hat{n}_s$ points to the right.

D. Discretization

We discretize using the usual MOM procedure, where the closed contour C consists of N straight-line segments, and a typical segment is depicted in Fig. 2, where $\overline{\rho}' = (x', y')$ is a coordinate along the contour, and ℓ_n, $\overline{\rho}^e_n = (x^e_n, y^e_n)$, $\overline{\rho}_n = (x_n, y_n)$, and $\hat{n}_{s,n}$ are the length, first endpoint, midpoint, and (body) outward normal, of the nth segment, respectively. Segments are connected such that $\hat{n}_{s,n}$ points to the right when moving from $\overline{\rho}^e_n$ to $\overline{\rho}^e_{n+1}$, i.e. the segments go counter-clockwise around the scatterer.

To find E_z and $\partial E_z / \partial n$, these unknowns are expanded in Region 0 as

$$E_{z0}(x, y) = \sum_{n=1}^{N} a_n f_n(x, y) \tag{22}$$

$$\frac{\partial E_{z0}(x, y)}{\partial n_s} = \sum_{n=1}^{N} b_n f_n(x, y) \tag{23}$$

where the point $\overline{\rho} = (x, y)$ lies on the contour C, and $f_n(x, y)$ is a pulse function giving 1 when (x, y) lies on segment n and 0 otherwise. Substituting into (10) and applying point matching at (x_m, y_m),

$$\sum_{n=1}^{N} a_n \delta_{mn} = E^{\text{inc}}_{z0}(x_m, y_m) - \sum_{n=1}^{N} a_n Q^{(0)}_{mn} + \sum_{n=1}^{N} b_n S^{(0)}_{mn} \tag{24}$$

where

$$Q^{(0)}_{mn} = \int_0^{\ell_n} \frac{\partial g_0 \left[x_m, y_m; x_n(\ell'), y_n(\ell') \right]}{\partial n'_s} d\ell' \tag{25}$$

$$S^{(0)}_{mn} = \int_0^{\ell_n} g_0 \left[x_m, y_m; x_n(\ell'), y_n(\ell') \right] d\ell' \tag{26}$$

and x and y along the contour segment are given by $p_n(\ell') = (p^e_{n+1} - p^e_n)\ell' + p^e_n$, with $p \in \{x, y\}$. The derivative of the Green's function in (25) can be evaluated directly as

$$\frac{\partial g_i}{\partial n'_s} = \frac{j k_{\rho i}}{4} \frac{H_0^{(2)\prime}(k_{\rho i} R)}{R} \left[n_{s,n,x}(x' - x) + n_{s,n,y}(y' - y) \right] \tag{27}$$

where $\hat{n}_{s,n} = n_{s,n,x} \hat{x} + n_{s,n,y} \hat{y}$ and $R = |\overline{\rho} - \overline{\rho}'|$.

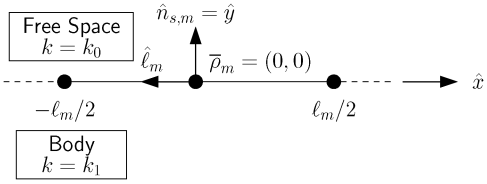

Fig. 3. Integration path for case of $m = n$, where segment is rotated and translated to the origin for convenience.

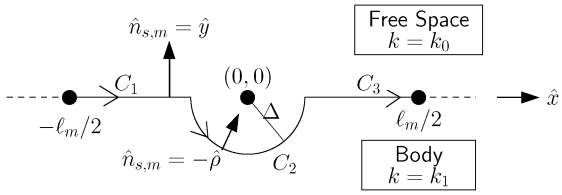

Fig. 4. Integration path for observing fields in Region 0 for the singular case of $m = n$, where segment is rotated and translated to the origin for convenience.

For $m \neq n$, we can approximate integrals in (24)–(26) as the integrand evaluated at the midpoint times the length of the segment, or

$$Q_{mn}^{(0)} \approx \frac{\partial g_0[x_m, y_m; x_n, y_n]}{\partial n_s'} \ell_n \tag{28}$$

$$S_{mn}^{(0)} \approx g_0(x_m, y_m; x_n, y_n)\ell_n. \tag{29}$$

For higher accuracy, multipoint numerical quadrature methods can also be applied.

For the case of $m = n$, the observation point is on the source segment, and the integral must be evaluated. Fig. 3 depicts the integration path for the case of $m = n$ where the segment has been rotated to align with the x-axis and translated to have its midpoint at the origin. We have

$$S_{mm}^{(0)} = \frac{j}{4} \int_{-\ell_m/2}^{\ell_m/2} H_0^{(2)}\left(k_{\rho 0}|x'|\right) dx' \tag{30}$$

$$= \frac{j}{2k_{\rho 0}} \int_0^{k_{\rho 0}\ell_m/2} H_0^{(2)}(u) du \tag{31}$$

which can be evaluated using the indefinite integral

$$\begin{aligned} s(u) &= \int H_0^{(2)}(u) du, \\ &= u H_0^{(2)}(u) \\ &\quad + \frac{1}{2}\pi u \left[T_0(u) H_1^{(2)}(u) - T_1(u) H_0^{(2)}(u)\right] \end{aligned} \tag{32}$$

where $T_0(u)$ and $T_1(u)$ are the Struve functions [12]. Since $\lim_{u\to 0} s(u) = 0$, we have

$$S_{mm}^{(0)} = \frac{j}{2k_{\rho 0}} s(k_{\rho 0}\ell_m/2). \tag{33}$$

For the evaluation of $Q_{mm}^{(0)}$, we avoid direct integration of the higher order singularity by changing the contour to be that depicted in Fig. 4, chosen such that the observation point at the middle of the interval is *inside* the complete contour C, and let $\Delta \to 0$. Along C_1, the contribution to $Q_{mm}^{(0)}$ is

$$\lim_{y\to 0} \frac{j}{4} \int_{-\ell_m/2}^{-\Delta} H_0^{(2)\prime}(k_{\rho 0} R) \frac{k_{\rho 0} y}{R} dx \tag{34}$$

where $R = \sqrt{x^2 + y^2}$, and (34) vanishes as does the contribution on C_3. Thus, only the integral on C_2 has a contribution, and recognizing $\hat{n}_{s,m} = -\hat{\rho}$,

$$Q_{mm}^{(0)} = -\lim_{\Delta\to 0} \frac{j}{4} \int_{\phi=-\pi}^{0} \left.\frac{\partial H_0^{(2)}(k_{\rho 0}\rho)}{\partial \rho}\right|_{\rho=\Delta} \Delta d\phi \tag{35}$$

$$= -\lim_{\Delta\to 0} \frac{1}{2\pi} \int_{\phi=-\pi}^{0} \left.\frac{\partial \ln(k_{\rho 0}\rho)}{\partial \rho}\right|_{\rho=\Delta} \Delta d\phi = -\frac{1}{2} \tag{36}$$

where the integral was performed from $-\pi$ to 0 to ensure that $d\ell = \Delta d\phi$ is positive and the logarithm came from the small argument approximation of the Hankel function.

In a similar way, the surface integral inside the body (12) is evaluated according to

$$\sum_{n=1}^{N} a_n \delta_{mn} = \sum_{n=1}^{N} a_n Q_{mn}^{(1)} - \sum_{n=1}^{N} b_n S_{mn}^{(1)} \tag{37}$$

where

$$Q_{mn}^{(1)} = \int_0^{\ell_n} \frac{\partial g_1\left[x_m, y_m; x_n(\ell'), y_n(\ell')\right]}{\partial n_s'} d\ell' \tag{38}$$

$$S_{mn}^{(1)} = \frac{c_{e,0}}{c_{e,1}} \int_0^{\ell_n} g_1\left[x_m, y_m; x_n(\ell'), y_n(\ell')\right] d\ell' \tag{39}$$

where (19) was combined with (23) to obtain $\partial E_{z1}/\partial n_s$. For $m \neq n$, single point numerical quadrature can be used as before. For the case of $m = n$, we have

$$S_{mm}^{(1)} = \frac{j c_{e,0}}{2k_{\rho 1} c_{e,1}} s(k_{\rho 1}\ell_m/2) \tag{40}$$

$$Q_{mm}^{(1)} = \frac{1}{2}. \tag{41}$$

Note that $Q_{mm}^{(1)}$ has the opposite sign as $Q_{mm}^{(0)}$, since for the required contour to enclose the observation point, it must circle around the top side of the singularity depicted in Fig. 4, and $\hat{n}_{s,m} = \hat{\rho}$.

Summarizing, (24) and (37) characterize the system, which can be written in matrix form as

$$\begin{bmatrix} \overline{\overline{I}} + \overline{\overline{Q}}^{(0)} & -\overline{\overline{S}}^{(0)} \\ \overline{\overline{I}} - \overline{\overline{Q}}^{(1)} & \overline{\overline{S}}^{(1)} \end{bmatrix} \begin{bmatrix} \overline{a} \\ \overline{b} \end{bmatrix} = \begin{bmatrix} \overline{v} \\ \overline{0} \end{bmatrix} \tag{42}$$

where $v_m = E_z^{\text{inc}}(x_m, y_m)$, and (42) can be inverted to find $\overline{a}$ and $\overline{b}$. Scattered E_z outside the body is given by

$$E_{z0}^{\text{scat}}(\overline{\rho}) = -\sum_{n=1}^{N} a_n Q_n^{(0)}(\overline{\rho}) + \sum_{n=1}^{N} b_n S_n^{(0)}(\overline{\rho}) \tag{43}$$

where

$$Q_n^{(0)}(\overline{\rho}) = \int_0^{\ell_n} \frac{\partial g_0\left[x, y; x_n(\ell'), y_n(\ell')\right]}{\partial n_s'} d\ell' \tag{44}$$

$$S_n^{(0)}(\overline{\rho}) = \int_0^{\ell_n} g_0\left[x, y; x_n(\ell'), y_n(\ell')\right] d\ell' \tag{45}$$

and analogous expressions can be derived for total field inside the body.

The procedure for finding H_z is identical to that for E_z, by simply making the substitutions

$$E_z(x, y) \rightarrow H_z(x, y) \tag{46}$$

$$E_z^{\text{inc}}(x_m, y_m) \rightarrow H_z^{\text{inc}}(x_m, y_m) \tag{47}$$

$$c_{e,0}/c_{e,1} \rightarrow c_{h,0}/c_{h,1} \tag{48}$$

in the above development.

After solution of E_z and H_z, transverse fields are given by (4) and (5), which in component form are

$$E_x = -\frac{j}{k_\rho^2}\left(k\eta \frac{\partial H_z}{\partial y} + k_z \frac{\partial E_z}{\partial x}\right) \tag{49}$$

$$E_y = -\frac{j}{k_\rho^2}\left(k_z \frac{\partial E_z}{\partial y} - k\eta \frac{\partial H_z}{\partial x}\right) \tag{50}$$

$$H_x = \frac{j}{k_\rho^2}\left(\frac{k}{\eta} \frac{\partial E_z}{\partial y} + k_z \frac{\partial H_z}{\partial x}\right) \tag{51}$$

$$H_y = \frac{j}{k_\rho^2}\left(k_z \frac{\partial H_z}{\partial y} - \frac{k}{\eta} \frac{\partial E_z}{\partial x}\right). \tag{52}$$

Transverse scattered field outside the body is found by substituting (43) and the analogous expression for H_z into (49)–(52). In this case, derivatives with respect to x or y can be transferred to $Q_n^{(0)}(\overline{\rho})$, and $S_n^{(0)}(\overline{\rho})$, or

$$\frac{\partial E_{z0}^{\text{scat}}(\overline{\rho})}{\partial p} = -\sum_{n=1}^{N} a_n \frac{\partial Q_n^{(0)}(\overline{\rho})}{\partial p} + \sum_{n=1}^{N} b_n \frac{\partial S_n^{(0)}(\overline{\rho})}{\partial p} \tag{53}$$

where $p \in \{x, y\}$,

$$\frac{\partial Q_n^{(0)}(\overline{\rho})}{\partial p} = \int_0^{\ell_n} \frac{\partial^2 g_0\left[x, y; x_n(\ell'), y_n(\ell')\right]}{\partial n_s' \partial p} d\ell' \tag{54}$$

$$\frac{\partial S_n^{(0)}(\overline{\rho})}{\partial p} = \int_0^{\ell_n} \frac{\partial g_0\left[x, y_m; x_n(\ell'), y_n(\ell')\right]}{\partial p} d\ell' \tag{55}$$

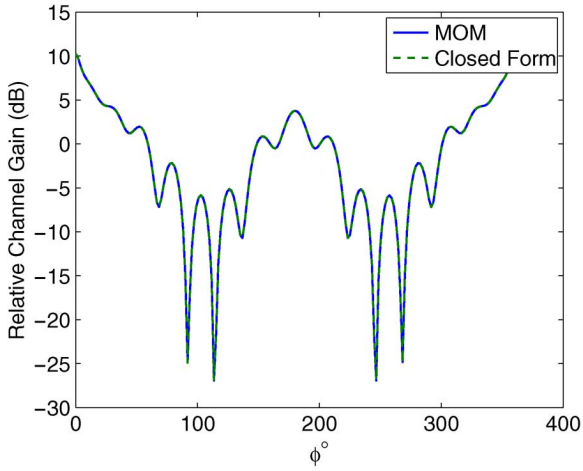

Fig. 5. Channel comparison of E_z in response to a z-directed line source.

and

$$\frac{\partial^2 g_0}{\partial n_s' \partial p} = -\frac{jk_{\rho 0}}{4}\Bigg\{\left[n_{s,n,x}(x - x') + n_{s,n,y}(y - y')\right] \times \left[Rk_{\rho 0} H_0^{(2)\prime\prime}(k_{\rho 0} R) - H_0^{(2)\prime}(k_{\rho 0} R)\right] \times \frac{(p - p')}{R^3} + n_{s,n,p} \frac{H_0^{(2)\prime}(k_{\rho 0} R)}{R}\Bigg\} \tag{56}$$

$$\frac{\partial g_0}{\partial p} = \frac{jk_\rho}{4} \frac{H_0^{(2)\prime}(k_\rho R)}{R}(p - p'). \tag{57}$$

E. Point Source

The electric and magnetic fields due to a line source near the lossy torso model derived in the previous sections can be transformed to a point source using the Fourier transform technique described in [5].

III. Validation and Torso Models

As a validation of the proposed BAN model for arbitrary cross section, the numerical method explained above is compared with the closed form solution for a circular cross section [6]. A lossy cylinder of radius $1.0\lambda_0$ and relative permittivity of $\epsilon_r = 2$ is used, and the source was placed at $\phi_0 = 0$ and $\rho_0 = 1.5\lambda_0$. The comparison for different orientation of receive/transmit sensor/source is shown in Figs. 5 and 6 where the fields (E_z and E_ρ) are compared at fixed observation radius $\rho = 1.6\lambda_0$ versus observation angle ϕ.

In order to correctly quantify path loss around the human body, the human torso shape should be accurately identified. A camera-based measurement system was used, where the subject stands on a circular disk which is turned to different angles in 10° increments and a photo is taken at each position. Comparing the width of the subject to a measured standard in the photo and properly accounting for the camera perspective allows the diameter of the subject versus rotation to be reliably estimated.

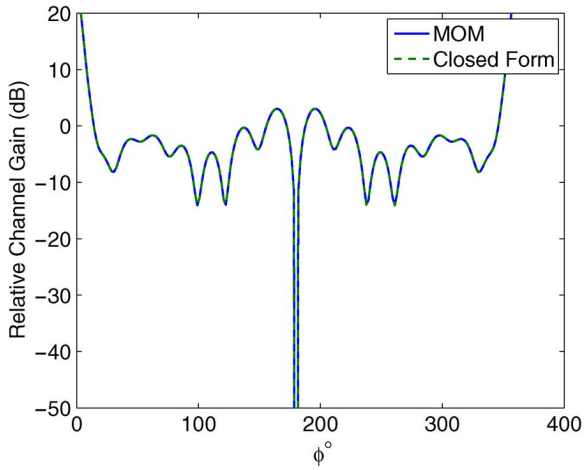

Fig. 6. Channel comparison of E_ρ in response to a ϕ-directed line source.

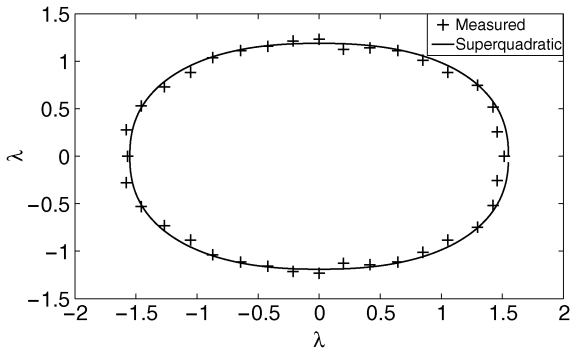

Fig. 7. Measured torso of the subject (in wavelengths).

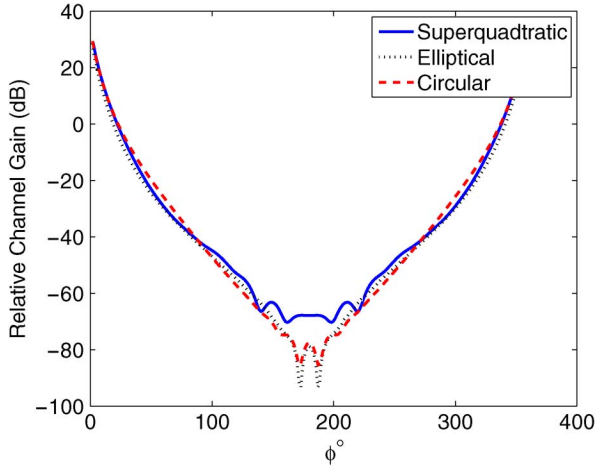

Fig. 8. Model comparison of E_z in response to a z-directed point source.

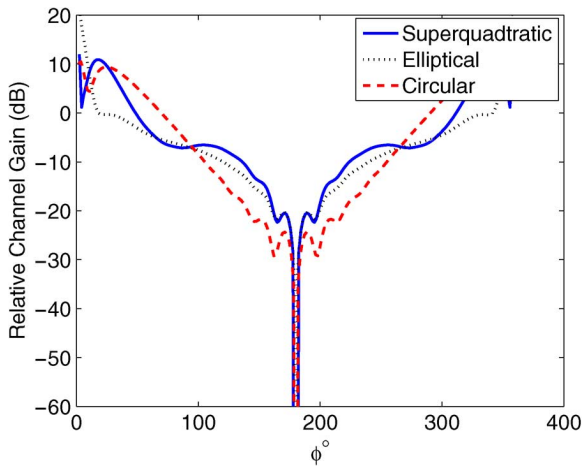

Fig. 9. Model comparison of E_ϕ in response to a ρ-directed point source.

The torso measurement result is shown in Fig. 7 which has axial length $\mathrm{a} = 1.55\lambda_0$ and $\mathrm{b} = 1.19\lambda_0$.

The human torso may be approximated by a superquadratic ellipse, given by

$$\left|\frac{x-x_0}{a}\right|^m + \left|\frac{y-y_0}{b}\right|^m = 1 \tag{58}$$

where a and b are the axial lengths, m is the exponent, and (x_0, y_0) is the center coordinate. In order to show that the specific shape of the body can make a significant difference in BAN modeling for certain polarizations, we also consider simplified circular and elliptical models. For all models, relative permittivity $\epsilon_r = 45.5 - j10.9$ was chosen to match average properties of fat (15%) and muscle (85%) at 2.55 GHz [13]. Also, the source was placed at $\phi_0 = 0$ and $\rho_0 = 1$ cm for $\hat{z}$ and $\hat{\phi}$ polarization and $\rho_0 = 3$ cm for $\hat{\rho}$ polarization. Model parameters are as follows:

Circular model: For the circular model, $m = 2$, and the radius is chosen to be $a = b = 1.42\lambda_0$ in order to have the same perimeter as the subject.

Elliptical model: The elliptical model has $m = 2$ and the same perimeter length as the measured torso, keeping a/b constant. This leads to $a = 1.59\lambda_0$, $b = 1.22\lambda_0$.

Superquadratic model: For the general superquadratic model $a = 1.55\lambda_0$, $b = 1.19\lambda_0$ and $m = 2.35$ are chosen to match the measured subject.

The electric field intensity as a function of angle ϕ at 2.55 xGHz for $z - z$ and $\phi - \rho$ polarization is shown in Figs. 8 and 9 respectively, where $p_1 - p_2$ polarization refers to $\hat{p}_1$-directed field in response to a $\hat{p}_2$-directed point current. The simulation shows that the propagation around the torso is nearly exponentially with distance (observation angle) and can be sensitive to the shape of the model, especially for cross polarization. Also, these figures shows some fluctuation (partial nulls) in the shadow region near the back of the torso which is explained by the interference of clockwise and counter-clockwise creeping waves.

IV. Body Area Networks Measurements

This section describes measurements conducted in the anechoic chamber in Fig. 10(a) and in an open range, indicating that the proposed method provides reasonable accuracy.

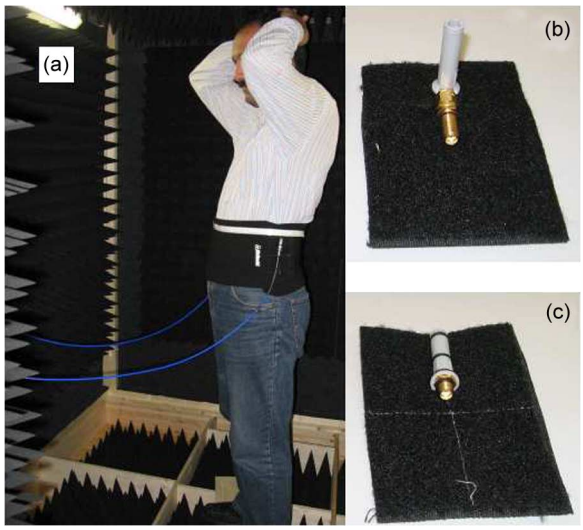

Fig. 10. Measurement of BAN channels: (a) anechoic chamber measurement with subject, (b) antenna for $\hat{\rho}$ polarization and (c) antenna for $\hat{z}$ and $\hat{\phi}$ polarizations.

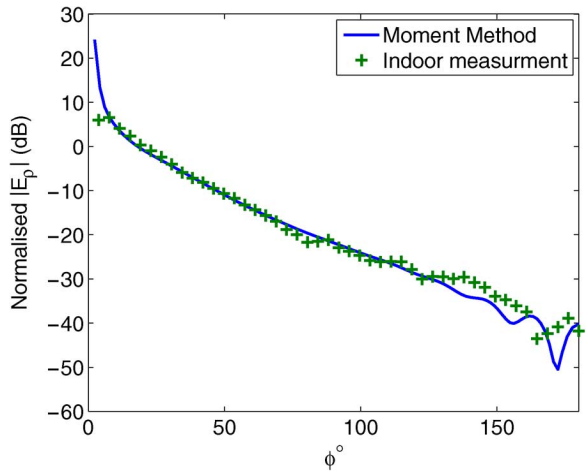

Fig. 11. Measurement and model comparison of E_ρ in response to a ρ-directed point source.

A. Network Analyzer-Based System

Measurements of the BAN channel were performed with a Rohde&Schwarz ZVB20 vector network analyzer connected to the antennas via 3 m instrument grade SMA cables (Mini-Circuits CBL-10FT-SMS+) and 20 dBm transmit power. During the measurements, the subject placed his hands over his head to reduce the influence of the arms. In the following study, one antenna was placed above the left hip of the subject and the other antenna starting above the right hip and moved in 1 cm increments around the waist toward the other antenna.

B. BAN Antenna

Fig. 10(b) and (c) depict the antennas that were used for the measurement, which are 1.5 cm monopoles. The monopoles were chosen to be short (approximately $\lambda/8$) compared to the wavelength λ at 2.55 GHz, thus approximating a point transmit current and a point receive field sensor. The matching efficiency of the short monopoles is between 0.1 and 0.5 depending on the orientation relative to the body, but the maximum additional link loss of 20 dB does not significantly hinder the short range BAN measurements.

Antennas were sewn onto small Velcro patches attached to an ordinary back-support Velcro band worn around the waist. To allow all combinations of the three transmit and receive polarizations to be measured, two antennas were constructed with right angle cable connections ($\hat{\rho}$ polarization) and two with straight connections ($\hat{\phi}$ and $\hat{z}$ polarization). A long Velcro measuring tape was attached to the waist strap allowing the antennas to be positioned with ± 1 mm accuracy.

When the antennas were very close (<3 cm), accurate placement was difficult due to the overlap of the Velcro bands, so some variation from the ideal response is expected. The circumference of the subject from the two extreme points above the hip was 47 cm. The thickness of the clothes and Velcro band together was estimated as 0.5 cm. The distance between the body and the antenna can significantly influence the pathloss and needs to be carefully determined. The additional displacement of the antennas from the body was 2.5 cm for $\hat{\rho}$ oriented and 0.5 cm for $\hat{z}$ and $\hat{\phi}$ oriented monopoles.

C. Anechoic Chamber and Outdoor Measurement

A small anechoic chamber was constructed for performing on-body measurements having dimensions 2.0 m for the width and length and 2.2 m for the height. The floor was constructed as an open lattice of thin planks, allowing microwave absorber to be placed between the planks and a human subject to stand over the absorber. The walls, floor, and ceiling are covered with EPP-22 absorber material from Telemeter Electronic GmbH, having a normal reflection below -40 dB in the 2–4 GHz band. Due to budget constraints, only the center 1.5 m $\times$ 1.5 m area of each surface was covered with absorber. Fig. 10(a) depicts the inside of the chamber with the human subject. As shown, the cables were oriented to hang parallel to the body, since having cables encircling the body had a strong influence on the measurements. Although channels were measured with a broadband 2 to 5 GHz sweep, only the results at 2.55 GHz are presented here.

Outdoor measurements of the $\hat{z}$ polarization were also carried out at the Jacobs University campus in a large open environment, where the nearest building from the measurement point is 70 m. Measurements were performed by covering the network analyzer with absorber to reduce the effect of reflections from the instrument. In addition, microwave absorber was placed on the ground around the subject.

D. Measurement and Model Comparison

Measurement results are now compared with the superquadratic model in Section III. Fig. 11 depicts the result for $\hat{\rho}$ oriented transmitter and receiver (antenna perpendicular to body). The model is able to accurately predict the field decay with increasing separation, as well as the presence of a small dip just before the most extreme separation.

Fig. 12 shows the result for $\hat{z}$ oriented transmitter and receiver (antenna parallel to body), which exhibits very high shadowing. A floor is seen in the measured power in the strongly shadowed

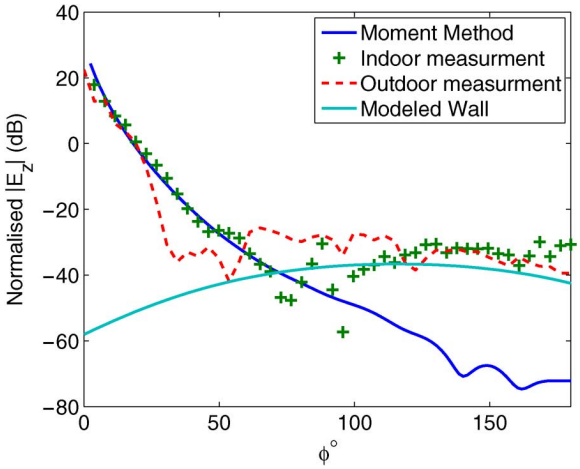

Fig. 12. Measurement and model comparison of E_z in response to a z-directed point source.

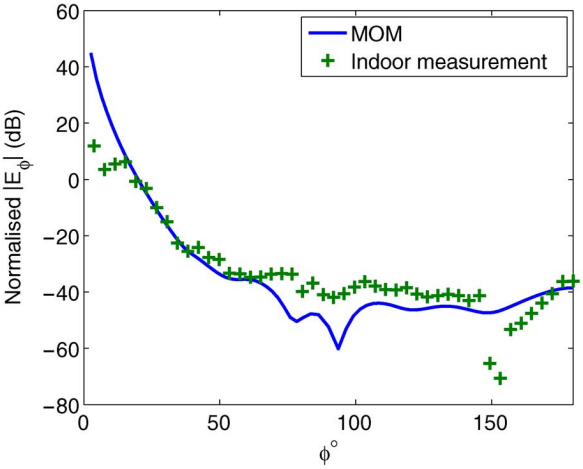

Fig. 13. Measurement and model comparison of E_ϕ in response to a ϕ-directed point source.

region, which we believe is due to wall or floor reflections. Comparison of the floor with a simulated wall reflection assuming a −40 dB reflection coefficient for the wall shows reasonable agreement. Unfortunately, outdoor measurements of the same polarization did not improve the accuracy of fit of the model, which could be resulting from the absorber around the subject's feet. These results reveal that performing BAN measurements for regions with strong shadowing are difficult, since reflections can easily overshadow on-body propagation mechanisms.

Fig. 13 compares the measurement and model for a $\hat{\phi}$-directed source and sensor. Although an initial discrepancy is seen due to placement constraints of the antennas, the overall trend is well captured, with the exception of an unexpected dip in the shadow region. Fig. 14 shows the result for a cross-polarization measurement, which is expected to be more sensitive to body shape and may be important for sensors that can be placed at arbitrary angle. Although the fit is not perfect, the trend is quite similar, where both the measurement and model predict higher initial decay, followed by a region of more gradual decay, ending with a sharp drop. The circular cylinder model is also shown for

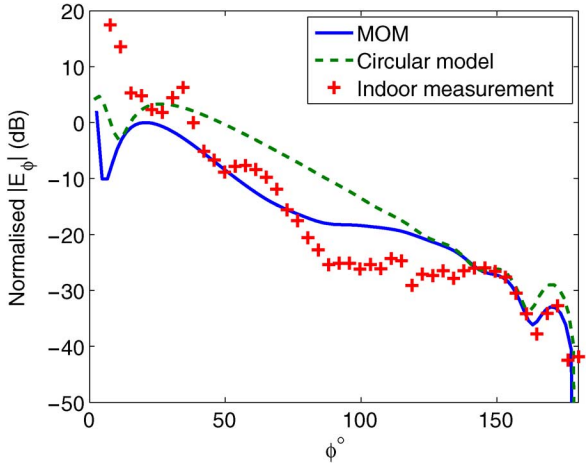

Fig. 14. Measurement and model comparison of E_ϕ in response to a ρ-directed point source.

comparison, which cannot predict the two initial decay regions with differing slopes.

V. Conclusion

This paper has developed an improved propagation model for body area networks, where the body is modeled as an infinite cylinder having an arbitrary cross section. Expressions for the fields around the body in response to a point source are obtained using an efficient surface-based method-of-moments formulation. The method was validated by comparison to the closed-form model of a circular cylinder.

Fields around the torso were simulated for three simple models indicating nearly exponential decay of the fields with distance on the body. Additionally, it was observed that some polarizations were sensitive to the shape of the body. The model was compared with on-body measurements performed in an anechoic chamber as well as an open field. Although reasonable agreement was obtained, results indicate that for certain polarizations, direct measurement is difficult in the shadow region due to weak reflections from chamber walls and other environmental effects.

References

[1] J. Ryckaert, P. De Doncker, R. Meys, A. de Le Hoye, and S. Donnay, "Channel model for wireless communication around human body," *Electron. Lett.*, vol. 40, pp. 543–544, Apr. 2004.

[2] T. Zasowski, F. Althaus, M. Stager, A. Wittneben, and G. Troster, "UWB for noninvasive wireless body area networks: Channel measurements and results," in *Proc. IEEE Conf. on Ultra Wideband Systems and Technologies*, Zurich, Switzerland, Nov. 16–19, 2003, pp. 285–289.

[3] A. Fort, C. Desset, J. Ryckaert, P. De Doncker, L. Van Biesen, and P. Wambacq, "Characterization of the ultra wideband body area propagation channel," presented at the IEEE Int. Conf. on Ultra-Wideband, Leuven, Belgium, Sep. 5–8, 2005.

[4] A. Alomainy, Y. Hao, X. Hu, C. Parini, and P. Hall, "UWB on-body radio propagation and system modelling for wireless body-centric networks," *IEE Proc. Commun.*, vol. 153, pp. 107–114, Feb. 2006.

[5] A. Fort, F. Keshmiri, G. Crusats, C. Craeye, and C. Oestges, "A body area propagation model derived from fundamental principles: Analytical analysis and comparison with measurements," *IEEE Trans. Antennas Propag.*, vol. 58, pp. 503–514, Feb. 2010.

[6] A. M. Eid, N. Murtaza, and J. W. Wallace, "Green's function models and measurements for body area network (BAN) channels," presented at the Proc. IEEE Int. Conf. on Wireless Information Technology and Systems (ICWITS'10), Honolulu, HI, Aug. 28–Sep. 3 2010.
[7] Y. Leviatan and A. Boag, "Analysis of TE scattering from dielectric cylinders using a multifilament magnetic current model," *IEEE Trans. Antennas Propag.*, vol. 36, pp. 1026–1031, Jul. 1988.
[8] E. Arvas and T. K. Sarkar, "RCS of two-dimensional structures consisting of both dielectrics and conductors of arbitrary cross section," *IEEE Trans. Antennas Propag.*, vol. 37, pp. 546–554, May 1989.
[9] M. A. Al-Kanhal and E. Arvas, "Electromagnetic scattering from a chiral cylinder of arbitrary cross section," *IEEE Trans. Antennas Propag.*, vol. 44, pp. 1041–1048, July 1996.
[10] J. Richmond, "Scattering by a dielectric cylinder of arbitrary cross section shape," *IEEE Trans. Antennas Propag.*, vol. 13, pp. 334–341, Mar. 1965.
[11] M. Sadiku, *Numerical Techniques in Electromagnetics*. Boca Raton, FL: CRC Press, 1992.
[12] Abramowitz and Stegun, *Handbook of Mathematical Functions*. Washington, DC: U.S. Dept. of Commerce, National Institute of Standards and Technology, 1965.
[13] "Dielectric Properties of Body Tissues" Italian National Research Council, Institute for Applied Physics [Online]. Available: http://niremf.ifac.cnr.it/tissprop/

Ahmed M. Eid was born in Egypt in 1974. He received the B.S. degree in electrical engineering from Zagazig University, Egypt, in 1997, the M.S. degree in communication engineering from Cairo University, Egypt, in 2006, and the Ph.D. degree in electrical engineering from Jacobs University, Bremen, Germany, in 2010.

From 2000 to 2007, he worked as a Vessel Traffic Management System (VTMS) Engineer for the Suez Canal Authority, and from 2007 to 2010 he was a Research Associate of the Wireless and Applied Electromagnetics Laboratory, Jacobs University Bremen. His research interests include antennas and microwave circuits, electromagnetic analysis and modeling, and microwave radar and sensing.

Jon W. Wallace (S'99–M'03) received the B.S. (*summa cum laude*) and Ph.D. degrees in electrical engineering from Brigham Young University (BYU), Provo, UT, in 1997 and 2002, respectively.

From 2002 to 2003, he was with the Mobile Communications Group , Vienna University of Technology, Vienna, Austria. From 2003 to 2006, he was a Research Associate with the BYU Wireless Communications Laboratory. Since 2006, he has been an Assistant Professor of electrical engineering at Jacobs University, Bremen, Germany. His current research interests include MIMO wireless systems, physical-layer security, cognitive radio, and body-antenna interactions.

Dr. Wallace is serving as an Associate Editor of the IEEE TRANSACTIONS ON ANTENNAS AND PROPAGATION.